Morphology-Control Synthesis of a Core−Shell Structured NiCu Alloy with Tunable Electromagnetic-Wave Absorption Capabilities

Biao Zhao,[†] Wanyu Zhao,[†] Gang Shao,*[,†] Bingbing Fan,[†] and Rui Zhang*[,†,‡]

[†]School of Materials Science and Engineering, Zhengzhou University, Zhengzhou 450001, China
[‡]Zhengzhou Institute of Aeronautical Industry Management, Zhengzhou 450046, China

S *Supporting Information*

ABSTRACT: In this work, dendritelike and rodlike NiCu alloys were prepared by a one-pot hydrothermal process at various reaction temperatures (120, 140, and 160 °C). The structure and morphology were analyzed by scanning electron microscopy, energy-dispersive spectrometry, X-ray diffraction, and transmission electron microscopy, which that demonstrate NiCu alloys have core−shell heterostructures with Ni as the shell and Cu as the core. The formation mechanism of the core−shell structures was also discussed. The uniform and perfect dendritelike NiCu alloy obtained at 140 °C shows outstanding electromagnetic-wave absorption properties. The lowest reflection loss (RL) of −31.13 dB was observed at 14.3 GHz, and the effective absorption (below −10 dB, 90% attenuation) bandwidth can be adjusted between 4.4 and 18 GHz with a thin absorber thickness in the range of 1.2−4.0 mm.

The outstanding electromagnetic-wave-absorbing properties are ascribed to space-charge polarization arising from the heterogeneous structure of the NiCu alloy, interfacial polarization between the alloy and paraffin, and continuous micronetworks and vibrating microcurrent dissipation originating from the uniform and perfect dendritelike shape of NiCu prepared at 140 °C.

KEYWORDS: *NiCu alloys, core−shell structure, dendrite-like shape, rod-like shape, microwave absorption, dielectric loss*
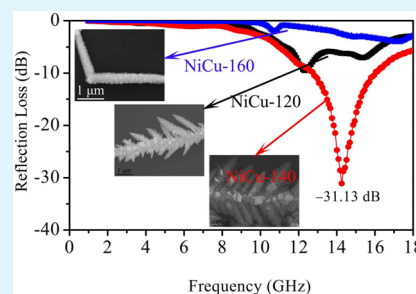
1. INTRODUCTION

Nowadays, serious invisible and omnipresent electromagnetic interference issues resulting from rapidly developing communication devices, such as mobile telephones, wireless Internet, and military application instruments, are absolutely harmful for the environment and human health. Moreover, this electromagnetic radiation plays a negative role in many sensitive electronic devices, which induces great degradation in their quality and interrupts their normal operation. Thus, it is urgently needed to explore new types of materials with high-efficiency electromagnetic-wave absorption.[1,2] Electromagnetic-wave-absorbing materials can absorb electromagnetic energy and convert it into thermal energy or other styles of energy through the cooperative action of magnetic loss or dielectric loss.[3,4] An ideal electromagnetic-wave-absorbing material should have the characteristics of thin thickness, low density, wide bandwidth, and strong absorption.[5,6]

A variety of materials, such as carbon-based,[7,8] metal magnetic,[9,10] organic polymer,[11] and semiconductor,[12,13] exhibit excellent electromagnetic-wave absorption properties in specific frequency ranges. On the basis of the loss mechanism of the electromagnetic energy, the absorbing materials could be classified into three categories, namely, the dielectric, magnetic, and resistance loss types.[14] Bimetallic alloys combining both the magnetic and dielectric loss types have shown a clear advantage in balancing the complex relative permittivity and permeability.[15−17] There are plentiful literatures concerning bimetallic ferromagnetic NiCo, FeNi, and FeCo used as electromagnetic-wave-absorbing materials with outstanding absorption proper-

ties. Yang and colleagues[18] prepared FeCo nanoplates by a chemical method, and the minimal reflection loss (RL) of the FeCo nanoplates was −43 dB at 8.1 GHz with an absorber thickness of 1.8 mm. Yu et al.[14] synthesized the leaflike hierarchical dendritic $Co_xFe_{1−x}$ (x = 0.1, 0.3, 0.5, and 0.7) alloys by an electrochemical reduction method under the electric field, and the leaflike dendritic $Co_{0.5}Fe_{0.5}$ alloy shows the strongest electromagnetic-wave absorption with a minimal RL of −59.1 dB. Wang et al.[19] fabricated sheetlike Co_3Fe_7 alloy-coated carbon fiber composites by electroplating with a minimal RL of −48.2 dB and a thickness of 1.7 mm. In our previous work,[20] one-dimensional chainlike CoNi alloys with excellent electromagnetic-wave absorption properties were fabricated via a tartrate-assisted hydrothermal method. The outstanding electromagnetic-wave absorption of −34.33 dB was observed at 17.5 GHz with a thickness of 1.0 mm. The excellent microwave absorption properties are ascribed to good impedance matching, multiple polarization, and a unique chainlike shape. Chen et al.[21] designed a porous FeNi nanocomposite using corncob powders as the template. The porous structure of the FeNi alloy can tune the permittivity (ε_r) and permeability (μ_r) to improve the impendence matching between the absorber and air, and the optimal RL values of porous FeNi absorbers is −40.8 dB. The above-mentioned research literature studies suggest that bimetallic alloys can be

utilized as potential electromagnetic-wave absorbing materials with features of strong absorption, wide bandwidth, and small thickness.

Noticeably, the morphologies of bimetallic alloys play a key role in determining the electromagnetic-wave absorption properties of the absorbers. Moreover, as far as we know, there are rare reports concerning NiCu alloys applied as electromagnetic-wave-absorbing materials. Zhang and Zeng[22] prepared one-dimensional NiCu nanowires by a solution-based epitaxial route, and the NiCu nanowires show ferromagnetic properties, which may be utilized as microwave through magnetic loss. The hybrid composites based on CuNi alloy nanoparticle-decorated natural graphite were synthesized through a simple reduction chemistry for electromagnetic interference shielding application by Kumari and co-workers.[23] In this work, dendritelike and rodlike core−shell-structured NiCu alloys were prepared by a facile one-pot hydrothermal process. These core−shell structures can induce space-charge and interfacial polarization, and unique dendritelike shapes can form a dissipation microcurrent and antenna receiver to absorb electromagnetic-wave energy. In addition, the ferromagnetic bimetallic NiCu alloys connecting dielectric and magnetic losses can enhance electromagnetic-wave absorption. In these views, this work is very promising.

2. EXPERIMENTAL SECTION

Raw Materials. All chemical reagents were commercially available and were used without further purification. Copper chloride hexahydrate ($CuCl_2 \cdot 2H_2O$), nickel chloride hexahydrate ($NiCl_2 \cdot 6H_2O$), and sodium hydrate (NaOH) were supplied by Xilong Chemical Reagent Co. Ltd. (Guangdong, China). Sodium hydrogen phosphate (NaH_2PO_2) and ethylenediamine ($H_2NCH_2CH_2NH_2$, EDA) were obtained from Tianjin Guangfu Reagent Corp. (Tianjin, China).

Preparation of a NiCu Alloy Composite. In a typical synthesis, the same amounts (1 mmol) of $CuCl_2 \cdot 2H_2O$ and $NiCl_2 \cdot 6H_2O$ were dissolved in 60 mL of a 2 M NaOH solution and kept for 30 min. Subsequently, 3 mL of EDA was added into the mixture. Then, an appropriate amount (10 mmol) of sodium hypophosphite mono-hydrate ($NaH_2PO_2 \cdot H_2O$) was introduced into the reaction mixture. The mixture was then transferred into a Teflon-lined autoclave. The autoclave was sealed and heated to a suitable temperature, maintained at this temperature for 15 h, and then cooled to room temperature. The black NiCu products were washed and filtered off with absolute ethanol and distilled water and then dried at 60 °C for 12 h under a vacuum. For convenience, the final NiCu samples synthesized at 120, 140, and 160 °C were denoted as NiCu-120, NiCu-140, and NiCu-160, respectively.

Characterization. The crystal structure and composition of as-received samples were analyzed by X-ray diffraction (XRD; Rigaku Ultima IV) using Cu Kα radiation. The microscopic morphology and microstructure of the NiCu alloys were observed by transmission electron microscopy (TEM; JEOL JEM-2100) at an acceleration voltage of 200 kV and field-emission scanning electron microscopy (FESEM; JEOL-7001F) associated with energy-dispersive spectrometry (EDS; Oxford, UK). The electromagnetic-wave absorption properties of the NiCu alloys with various morphologies were studied through a network analyzer (Agilent N5244A) in the frequency range of 1−18 GHz. The specimens applied for the electromagnetic measurements were prepared by homogeneously blending the NiCu alloys with paraffin wax (the weight ratio of the NiCu alloys was around 40%), and then the mixture was pressed into a ring shape (outer diameter of 7 mm and inner diameter of 3.04 mm). The relative complex permittivity ($\varepsilon_r = \varepsilon' - j\varepsilon''$) and permeability ($\mu_r = \mu' - j\mu''$) were obtained by the experimental scattering parameters S_{11} and S_{21} through the standard Nicolson−Ross theoretical calculations.[24]

3. RESULTS AND DISCUSSION

The phase and purity of the as-prepared NiCu products were examined by XRD, as shown in Figure 1. The XRD curves in
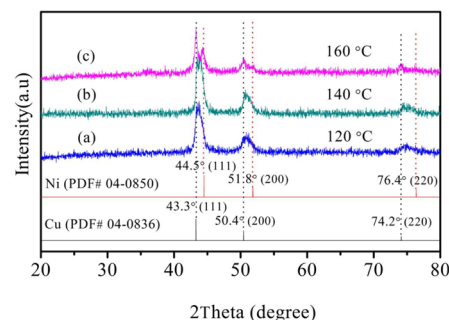

Figure 1. XRD patterns of (a) NiCu-120, (b) NiCu-140, and (c) NiCu-160 alloy samples and standard Cu and Ni from JCPDS files.

Figure 1a,b reveal the single face-centered-cubic (fcc) structures of the bimetallic NiCu alloys prepared at 120 and 140 °C, respectively. The diffraction peaks located between the standard copper and nickel (JCPDS 04-0836 and 04-0850) indicate the mutual insertion of copper and nickel atoms.[25] Upon further observation of Figure 1c, one can see that the diffraction peaks can be well-indexed to the mixture phases of Cu and Ni when the hydrothermal reaction was under a temperature of 160 °C. From the profiles of XRD, it can be found that the diffraction peaks of Ni in the NiCu composite become strong and obvious with increasing hydrothermal temperatures. Such a phenom-enon may be assigned to the different standard reduction potentials of Cu and Ni.[22] Moreover, no evidence of impurities is found in the XRD patterns of the three samples. These results indicate that the crystal compositions of the final NiCu products were vitally determined by hydrothermal temper-atures.

The morphology and microstructure of the NiCu alloy composite synthesized at 140 °C were examined by FESEM and TEM. Parts a and b of Figure 2 exhibit the representative FESEM images of a dendritelike NiCu alloy obtained at 140 °C
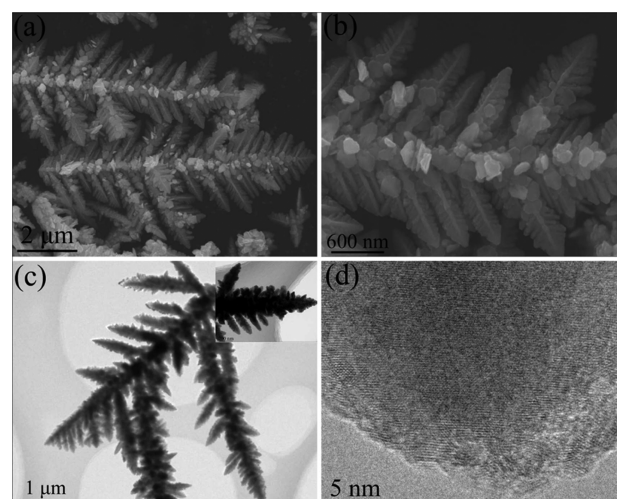

Figure 2. (a) Low-magnification and (b) high-magnification FESEM photographs, (c) TEM image, and (d) HRTEM image of a dendritelike NiCu alloy composite prepared under a temperature of 140 °C. Inset of part c: HRTEM image of a dendritelike NiCu alloy.

for 15 h. The alloys are hierarchical dendritelike micro-structures with width and length of about 2−3 and 9−12 μm, respectively. Upon further observation of the high-magnifica-tion image (Figure 2b), it is seen that a single leaf is comprised of dendritic fractal structures with a pronounced trunk and highly ordered branches distributed on both sides of the stem. Moreover, this dentritelike structure is duplicated in a smaller size on each branch. Figure 2c presents a TEM image of an individual dentritelike microstructure that reveals distinct dendritic microleaf structures. Further structural character-ization was analyzed by high-resolution TEM (HRTEM; Figure 2d). Owing to the diffusion of Ni atoms into the Cu lattice, causing a rearrangement of the Cu atoms, the 5-fold twinned crystal structure turned into a distorted or polycrystalline structure after alloying.[26] To verify the core−shell structure of the NiCu alloy, the high-quality TEM images were provided in Figure S1 in the Supporting Information (SI). From Figure S1 in the SI, the core−shell structure of NiCu alloys can be clearly observed.

To get more information on the leaflike NiCu alloy microstructure, the EDS technique were carried out, and the results are presented in Figure 3. Figure 3 show a single
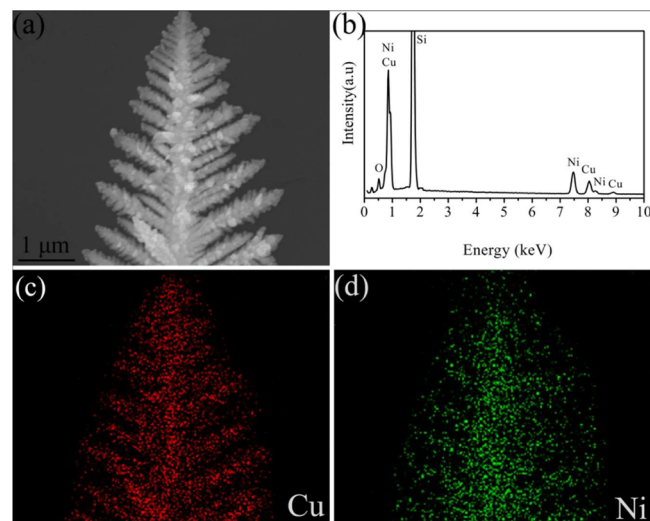

Figure 4. (a and b) FESEM images of the dendritelike NiCu alloy composite prepared at 120 °C. (c and d) FESEM photographs of the rodlike NiCu alloy composite synthesized at 160 °C.

Figure 3. (a) SEM photograph, (b) EDS profile, and (c and d) elemental mappings of Cu and Ni corresponding to the single dendritic NiCu alloy microleaf obtained at 140 °C.

Figure 4a,b, the low-magnification FESEM image (Figure 4a) reveals that the as-obtained products at 120 °C are composed of the plentiful dendritelike structures, indicating high yields, that are similar to the products prepared at 140 °C (Figure 2). However, upon close observation of the high-magnification SEM image (Figure 4b), it can be found that the branch surface of NiCu-120 microdendrites is rougher than that of NiCu-140 microdendrites and the NiCu-140 microdendrites grow more uniformly than the NiCu-120 microdendrites, which is due to the low driving energy of the nucleation of grains of low temperature. With increasing reaction temperature to 160 °C, interestingly, a majority of the rodlike products appear in the final NiCu alloys (Figure 4c), which are completely different from the products prepared at 120 and 140 °C. The nanorods are straight with diameters in the range of 100−200 nm (Figure 4d). The as-received nanorods are very long, possessing lengths of more than several tens of micrometers. From the above analysis, it can be inferred that the morphologies of NiCu alloys were largely affected by the hydrothermal temperature. It is well-known that the temperature provides the drive energy for nucleation of grains already formed and growth. At the low temperature (120 °C), the low drive energy cannot supply enough energy to make the microdendrites uniform and perfect compared with NiCu-140. The mechanism for the formation of dendritelike microstructures was similar to those of other groups' work.[27,28] Figure S2 in the SI shows the as-obtained products prepared without Ni^{2+} at 140 °C, while other synthesis parameters are constant. It can be clearly seen that the products consist of a dendritic Cu crystal, which validates dendritelike NiCu. In NiCu alloys, the dendritic Cu crystal was formed first and was regarded as the template to produce core−shell dendritelike NiCu alloys. At high temperature (160 °C), the rodlike structures rather than the leaflike structures are presented in the final products. It is not entirely clear why this transformation in the shape of NiCu alloys took place, but it is associated with the different growth directions between Ni and Cu.[22]

The dendrite NiCu-120 alloy was further characterized by high-magnification FESEM and EDS, and the results are exhibited in Figure 5a,b. It can be clearly seen that dendritelike products are composed of plentiful branches (Figure 5a). The

dendritic NiCu alloy and the corresponding elemental mappings of Cu and Ni. From Figure 3b, there are mainly Cu and Ni elements, except a small amount of O, in dendritelike CuNi alloys. Parts c and d of Figure 3 exhibit the elemental mappings of Cu and Ni, respectively. Both the Cu and Ni atoms uniformly distributed in agreement with the morphology of the dendritelike structure, which means that there is a homogeneous phase in the NiCu alloy. However, it is noted that the areas of Ni were bigger than those of Cu correspondingly, which indicates that Cu was in the core of the leaf and Ni was located in the shell, creating a special core−shell alloy.

To uncover the influence of the hydrothermal temperatures on the morphologies of NiCu alloy composites, two other temperatures (120 and 160 °C) were carried out while keeping other preparation parameters constant. Figure 4 shows the different magnification FESEM images of NiCu alloys synthesized at temperatures of 120 and160 °C. As shown in
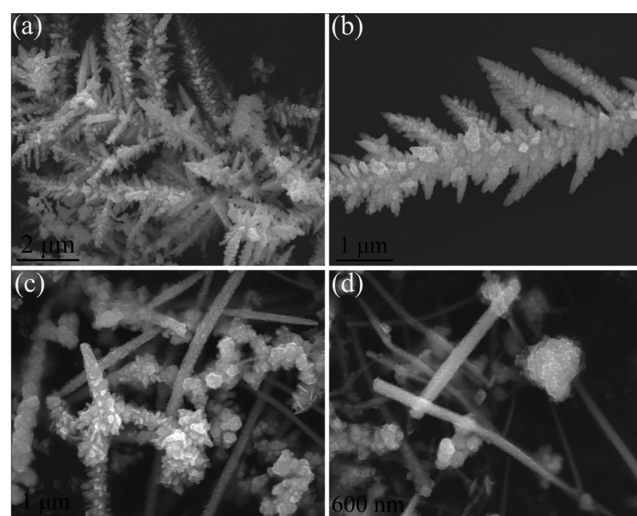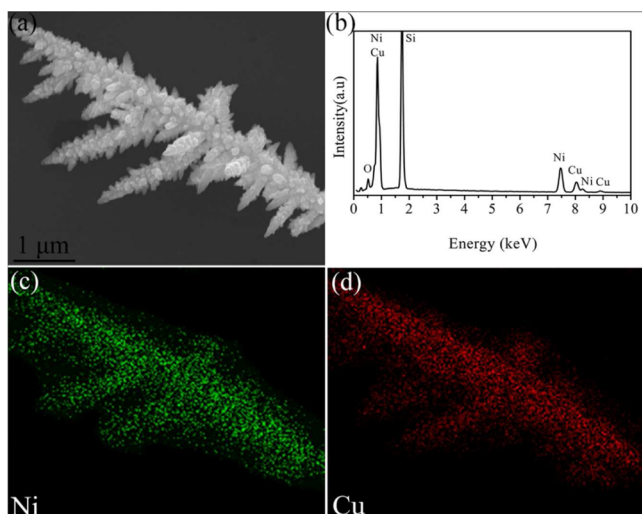
Figure 5. (a) SEM image, (b) EDS curve, and (c and d) elemental mappings of Ni and Cu corresponding to the single dendritelike NiCu alloy obtained at 120 °C.

EDS curve of the NiCu alloy composite indicates that the as-obtained NiCu-120 alloys are made up of Ni and Cu elements. The existence of a Si peak comes from the Si slice to support the samples during observation. Parts c and d of Figure 5 reveal the elemental mappings of NiCu-120 alloys. The Cu element can be clearly seen in the core area, while the Ni element is shown in the shell region. This validates core−shell structures of the NiCu alloy composite.

The EDS pattern and elemental mappings of rodlike NiCu-160 alloys are also demonstrated in Figure 6. There are mainly
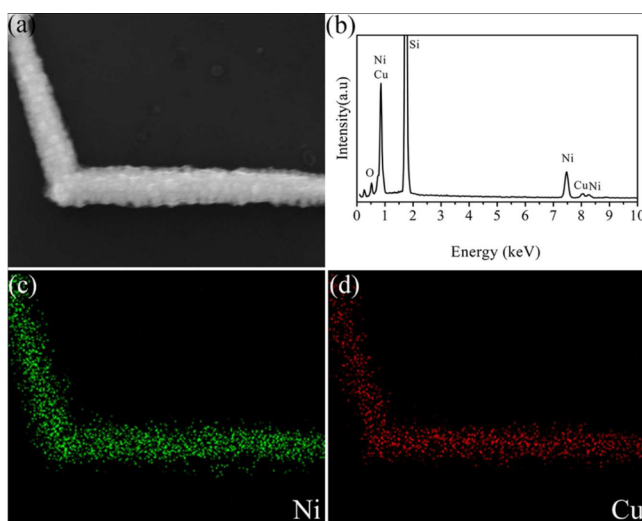

Figure 6. (a) SEM image, (b) EDS curve, and (c and d) elemental mappings of Ni and Cu corresponding to the rodlike NiCu alloys obtained at 160 °C.

Ni and Cu elements in the rodlike NiCu-160 sample. The elemental mappings of Ni and Cu are exhibited in Figure 6c,d. The Ni area is larger than the Cu area. This also verifies the core−shell nature of the rodlike NiCu-160 alloy composite.

To get bimetallic core−shell microstructures, the two metal ions should be deoxidized separately in the reaction. The core−shell microstructures are generated by the following process. One metal (M_2) ion was first deoxidized to form the core, and

then another M_1 was nucleated on the surface of M_2. It is also possible for heterogeneous nucleation of M_1 particles on the surface of M_2 nanoparticles to take place because the free energy needed for homogeneous nucleation of the single M_1 nanoparticles is larger than that of heterogeneous nucleation of the M_1 particles on the M_2 surface.[29,30] The core−shell bimetallic materials could be effectively generated on the basis of separate reduction reactions in two stages through the heterogeneous nucleation method mentioned above. In this work, complexes such as $Cu(EDA)_2^{2+}$ and $Ni(EDA)_3^{2+}$ are supposed to be occurring in solution precursors based on the coordination chemistry of the two metals.[31,32] The standard reduction potential of nickel $[E^0(Ni^{2+}/Ni^0) = -0.257 \text{ V}]$ is lower than that of copper $[E^0 (Cu^{2+}/Cu^0) = 0.342 \text{ V}]$.[22,33] Thus, copper is thus more easily reduced in competitive redox reactions. Because of the their widely differing redox potentials, in the mixture of Cu^{2+} and Ni^{2+} in EDA complexes, Cu−Ni core−shell microstructures were produced via the reduction of Ni^{2+} at relatively high temperature after Cu core small-particle generation at relatively low temperature.

It is commonly accepted that the electromagnetic-wave absorption properties of materials are mainly associated with the complex relative permeability $(\mu_r = \mu' - j\mu'')$ and permittivity $(\varepsilon_r = \varepsilon' - j\varepsilon'')$ as well as their microstructures.[34,35] The complex relative permeability and permittivity of paraffin-based samples containing dendritelike core−shell NiCu (NiCu-120 and NiCu-140) and rodlike core−shell-structured NiCu (NiCu-160) as fillers are measured through a vector network analyzer in the frequency range of 1−18 GHz (Figure 7). Parts a and b of Figure 7 exhibit the real (ε') and imaginary (ε'') parts of the complex permittivities of NiCu-120, NiCu-140, and NiCu-160 alloys. Notably, the ε' and ε'' values of NiCu-140 are larger than those of NiCu-120 and NiCu-160. Generally, the imaginary (ε'') and real (ε') parts are associated with dissipation of the electromagnetic energy and amount of polarization existing in the material under the alternating electromagnetic fields.[36] The relative high ε' and ε'' values of the NiCu-140 alloy indicate the high storage and loss ability of the microwave energy. The dielectric properties of the material are dependent on the space-charge polarization (heterogeneous structure in the system) and ionic, electronic, and dipole polarizations (the presence of dipoles).[37] However, the electronic and ionic polarizations were not considered because the two-polarization phenomenon usually occurs in the ultraviolet or IR frequency range.[38] According to the free-electron theory,[39] $\varepsilon'' \approx 1/\pi\varepsilon_0\rho f$, where ρ is the resistivity, it can be deduced that high ε'' means low resistivity. From the above results, it can be deduced that uniform and perfect leaflike NiCu alloys have relatively high conductivity, which may arise from the formation of a microcurrent under alteration of the electromagnetic field.[40] In general, a suitable electrical conductivity is favorable for enhancement of the electromagnetic-wave absorption abilities.[41] Moreover, the ε' and ε'' values of the three NiCu alloy samples show fluctuation in the entire frequency. Such phenomena, attributed to dipole polarization, cannot catch up with the electric field change at high frequencies.[42] Notably, the similar shapes of dendritelike NiCu-120 and NiCu-140 show the same trend in the complex permittivity, which is absolutely different from the rodlike NiCu-160 alloy. Furthermore, for the ε'' values, the relaxation of NiCu may stem from interfacial polarization. The interfacial dipoles mainly result from the core−shell structure, which exists among Ni and Cu interfaces.[43] The resonance peaks
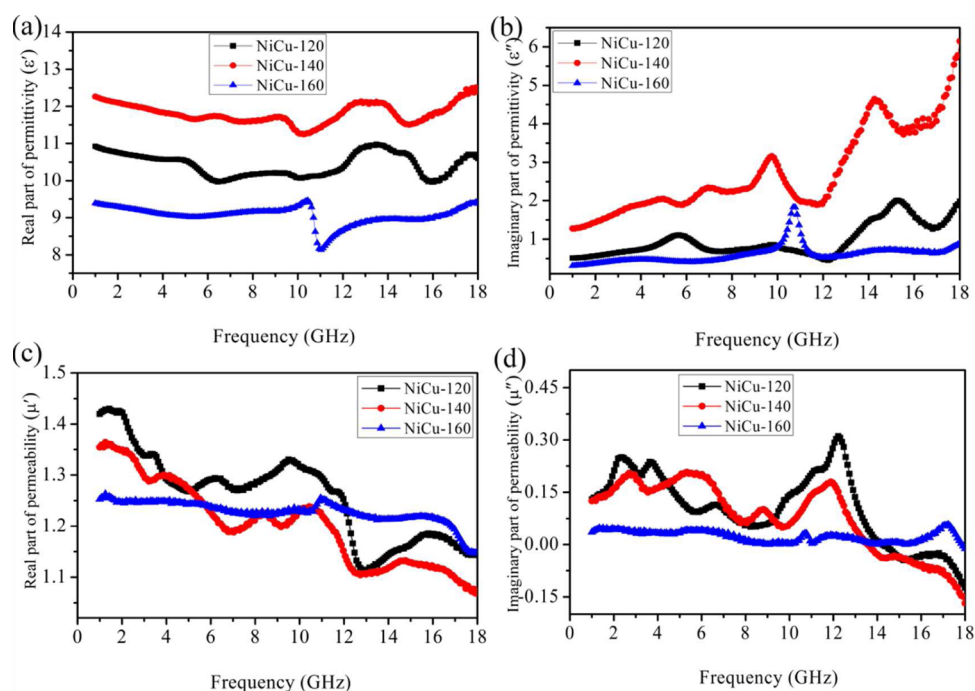
Figure 7. Frequency dependences of the (a) real and (b) imaginary parts of complex permittivity and the (c) real and (d) imaginary parts of complex permeability for various NiCu alloy composites prepared at different temperatures.

(Figure 7d) observed in the complex permeability are expected to be correlated with local confinement, natural resonance, and exchange resonance loss.[44]

The real (μ') and imaginary (μ'') parts of complex relative permeability of the three NiCu sample−paraffin composites are shown in parts c and d of Figure 7, respectively. For the real parts (μ'), it can be seen that three NiCu alloys show the decline tendency in the whole measured frequency of 1−18 GHz (Figure 7c). The μ' values of the NiCu-120, NiCu-140, and NiCu-160 alloys are in the ranges of 1.12−1.42, 1.07−1.36, and 1.16−1.27, respectively. For the leaflike NiCu-120 and NiCu-140 alloy samples, the μ'' values exhibit strong fluctuation in the entire frequency of 1−18 GHz, and a strong resonance can be observed at around 12 GHz in NiCu-120 and NiCu-140, which is ascribed to the unique dendritelike microstructures.[14] For the NiCu-160 sample, the μ'' value is in the range of 0.01−0.10 with negligible fluctuation. Notably, the μ'' value is less than zero in the 14−18 GHz range for the leaflike NiCu-120 and NiCu-140 samples, which is attributed to the electromagnetic field-induced eddy current. The eddy current will induce additional magnetic fields, which cancel the external magnetic field, causing negative permeability.[45] Moreover, from Figure 7b,d, it is noted that the change trend of the permittivity is just inverse to the permeability. The negative μ'' indicates that the magnetic energy is given out and converted to the electric energy, which can greatly enhance ε'' and then results in negative μ''.[46]

The magnetic loss tangent (tan $\delta_\mu = \mu''/\mu'$) and dielectric loss tangent (tan $\delta_\varepsilon = \varepsilon''/\varepsilon'$) are universally applied to evaluate the loss capacity of the microwave energy.[4,47] The high values of tan δ_μ and tan δ_ε mean high magnetic and dielectric losses. Parts a and b of Figure 8 depict the dielectric loss tan δ_ε and magnetic loss tan δ_μ for the core−shell NiCu alloys, respectively. As shown in Figure 8, the leaflike core−shell-structured NiCu-140 alloy possesses higher dielectric loss and relatively high dielectric loss compared with the other two
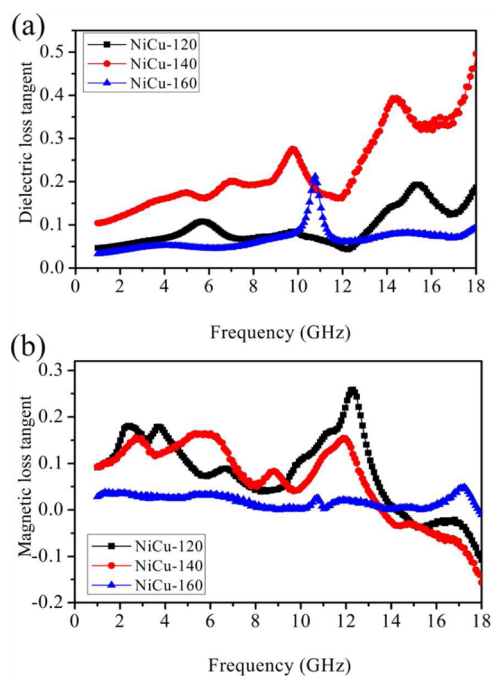

Figure 8. (a) Dielectric and (b) magnetic loss factors of core−shell NiCu alloy paraffin composites versus frequency.

samples NiCu-120 and NiCu-160. On the basis of the above results, it can be deduced that the dendritelike core−shell NiCu alloys (NiCu-120 and NiCu-140) have better loss abilities of the microwave energy than the rodlike core−shell NiCu alloy (NiCu-160).

Because of the heterogeneous systems of core−shell NiCu alloys, the migrating charges existing at the interface of Ni and Cu give rise to interfacial polarization, which is known as Maxwell−Wagner polarization.[48] It is well-known that inter-
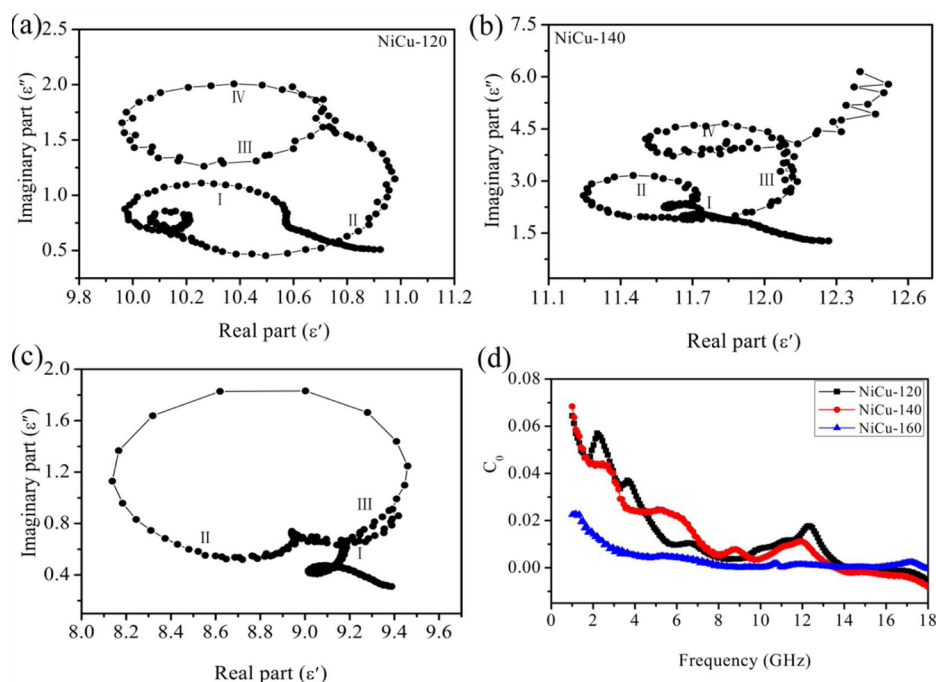
Figure 9. (a−c) Typical Cole−Cole semicircles (ε'' vs ε') for three core−shell NiCu alloy composites in the frequency range of 1−18 GHz. (d) Value C_0 $[\mu''(\mu')^{-2}f^{-1}]$ of NiCu alloy composites as a function of the frequency.

facial polarization and its associated relaxation will favor the electromagnetic-wave absorption property, which can be validated by the Cole−Cole semicircle.[49,50] On the basis of Debye dipolar relaxation, the relative complex permittivity can be described by the following equation:[51,52]

$$\varepsilon_r = \varepsilon_\infty + \frac{\varepsilon_s - \varepsilon_\infty}{1 + j2\pi f\tau} = \varepsilon' - j\varepsilon'' \tag{1}$$

where ε_s, ε_∞, and τ are the static dielectric constant, dielectric constant at infinite frequency, and polarization relaxation time, respectively. From eq 1, it can be deduced that

$$\varepsilon' = \varepsilon_\infty + \frac{\varepsilon_s - \varepsilon_\infty}{1 + (2\pi f)^2\tau^2} \tag{2}$$

$$\varepsilon'' = \frac{2\pi f\tau(\varepsilon_s - \varepsilon_\infty)}{1 + (2\pi f)^2\tau^2} \tag{3}$$

As inferred from eqs 2 and 3, we can obtain the relationship between ε' and ε'':

$$\left(\varepsilon' - \frac{\varepsilon_s + \varepsilon_\infty}{2}\right)^2 + (\varepsilon'')^2 = \left(\frac{\varepsilon_s - \varepsilon_\infty}{2}\right)^2 \tag{4}$$

Therefore, the curve of ε' versus ε'' is a single semicircle, which is generally called the Cole−Cole semicircle, and each semicircle is correlated with one Debye relaxation process.[53] Parts a−c of Figure 9 show the Cole−Cole semicircles (ε'' vs ε') for three core−shell NiCu alloy composites in the frequency range of 1−18 GHz, from which four Cole−Cole semicircles are observed for the dendritelike NiCu alloys (NiCu-120 and NiCu-140) and three semicircles existing in the rodlike NiCu-160 alloy. These results demonstrate that multiple dielectric relaxation processes take place in the NiCu alloy, which is ascribed to the core−shell structure and unique dendritelike and rodlike shapes. According to the Cao and co-workers reports,[54−56] the relaxations originate from the interfacial

polarizations among core−shell alloys, as well as the dipole polarizations caused by the defect dipole induced by the existence of an unbalanced charge between Ni and Cu lattices when the alloy absorbers are under an electromagnetic field. These shapes can provide large surface area and tune the complex permittivity, which allow the electromagnetic wave to enter the absorber as much as possible, namely, called a good impedance match.[2]

In general, the magnetic loss of microwave-absorbing material is mainly sourcing from the hysteresis loss, domain wall resonance, eddy current effect, and natural resonance.[57] Because of the weak electromagnetic field, the hysteresis loss can be excluded.[58] The magnetic domain wall resonance can be neglected because its contribution at microwave frequency is very small.[59] Therefore, the electromagnetic loss of the NiCu alloy was primarily attributed to the eddy current effect or natural resonance. If NiCu magnetic loss results from the eddy current effect, then C_0 $[C_0 = \mu''(\mu')^{-2}f^{-1} = 2\pi\mu_0\sigma d^2/3]$ should be constant.[60] The values of $C_0[\mu''(\mu')^{-2}f^{-1}]$ versus measured frequency of three NiCu alloys are presented in Figure 9d. However, the value decreases with increasing frequency. Thus, the magnetic loss of NiCu alloys was mainly originating from the natural resonance.

In order to obtain the high-efficiency electromagnetic-wave absorption properties, there are two points that should be considered. One is the impedance match, which makes the electromagnetic wave enter the interior of the absorber as much as possible. The other factor is the electromagnetic-wave attenuation in the interior of the absorber. The attenuation constant α, determining the dissipation properties of electromagnetic-wave-absorbing materials, can be expressed by[61,62]

$$\alpha = \frac{\sqrt{2}\,\pi f}{c}$$

$$\times \sqrt{(\mu''\varepsilon'' - \mu'\varepsilon') + \sqrt{(\mu''\varepsilon'' - \mu'\varepsilon')^2 + (\mu'\varepsilon'' - \mu''\varepsilon')^2}} \tag{5}$$

where f and c are the frequency and velocity of light, respectively. Figure 10 shows the attenuation constant α of
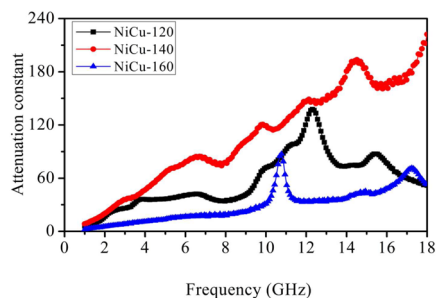

Figure 10. Attenuation constant of three core−shell NiCu alloy paraffin composites versus frequency.

three samples in the frequency range of 1−18 GHz. It is noticeable that the NiCu-140 paraffin composite possesses the largest attenuation constant among the three samples in the measured frequency range, which validated its outstanding absorption.

To evaluate the microwave absorption properties of three NiCu alloys with different shapes, the RL (the lower the value, the stronger the absorption), which was used to judge the absorption abilities of the absorber, can be calculated according to the relative permeability and permittivity with the given frequency and absorber thickness, through the following equation:[63,64]

$$RL = 20 \log |(Z_{in} - Z_0)/(Z_{in} + Z_0)| \tag{6}$$

$$Z_{in} = Z_0 \sqrt{\frac{\mu_r}{\varepsilon_r}} \tanh\left(j\frac{2\pi f d \sqrt{\mu_r \varepsilon_r}}{c}\right) \tag{7}$$

where Z_0 is the impedance of free space, Z_{in} the input impedance of the absorber, f the measured frequency, c the velocity of electromagnetic waves in free space, μ_r the complex relative permeability, ε_r the complex relative permittivity, and d the thickness of the absorber. The results are presented in Figure 11. Figure 11a shows the RL curves of NiCu-120, NiCu-140, and NiCu-160 paraffin composites with 40 wt % loading and a thickness of 2.0 mm. The NiCu-140 alloy shows stronger electromagnetic-wave absorption properties than the NiCu-120 and NiCu-160 alloys. The minimal RL of NiCu-140 is −15.39 dB at 10.1 GHz. Interestingly, the optimal RL of the three core−shell NiCu alloys can be observed at around 10 GHz, which may stem from the natural absorption properties of the NiCu alloys.[23] It can be also seen that there is a small difference in the RL curves, which is due to the influence of the various shapes of the three NiCu alloys. From the above equations, the thickness of the absorbing materials will affect the values of RL and the location of maximum absorption. Hence, the RLs of the three NiCu samples with different thicknesses were also calculated. Compared with NiCu-120 (Figure 11b) and NiCu-160 (Figure 11d), NiCu-140 (Figure 11c) reveals outstanding electromagnetic-wave absorption properties. As shown in Figure 11c, the minimal RL of −31.13 dB can be observed at 14.3 GHz and the bandwidth with the RL below −10 dB can reach 3.4 GHz (12.7−16.1 GHz) with a thickness of only 1.5 mm. The electromagnetic-wave absorption bandwidth with the RL below −10 dB can be adjusted from 4.4 to 18 GHz for the absorber with a thin thickness of 1.2−4.0 mm. Notably, with increasing thickness, the frequency corresponding to the minimal RL peaks would move toward low frequencies and two RL peaks would be observed with increasing thickness of more than 4.0 mm. This can be well explained by the quarter-wavelength cancellation model.[34,65]
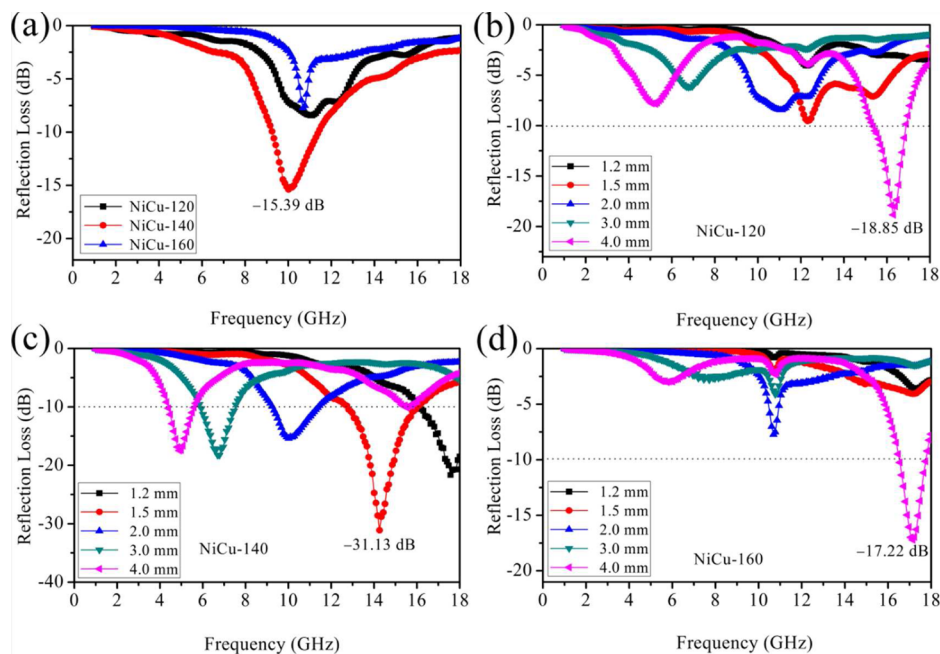

Figure 11. (a) RL curves of NiCu-120, NiCu-140, and NiCu-160 paraffin composites with 40 wt % loading and a thickness of 2.0 mm. (b−d) RL curves of 40 wt % NiCu-120, NiCu-140, and NiCu-160 wax composites at various thicknesses in the frequency range of 1−18 GHz.

The excellent electromagnetic-wave absorption of the core–shell dendritelike NiCu alloy can be attributed to good impedance match, multiple polarization relaxation, dielectric loss, and natural resonance. Besides the above-mentioned factors, the unique dendritelike structure is also helpful for the improvement of electromagnetic-wave absorption. First, connections between leaflike particles could lead to the formation of continuous micronetworks and vibrating micro-current when radiated from the alterative electromagnetic field. Second, dendritelike structures can act as quasi-antenna receivers, benefiting from the penetration of electromagnetic waves into the absorbers.[40] However, for the imperfect dendritelike NiCu-120 and rodlike NiCu-160, low fillers of NiCu alloys in the paraffin composites cannot link with each other, which results in relatively high resistivity, and the conduction loss (important dielectric loss in the metal materials) would be negligible. These results suggest that the electromagnetic-wave absorption capabilities of NiCu alloys can be tuned by control of the morphologies of the NiCu products.

4. CONCLUSION

In summary, the dendritelike and rodlike NiCu alloys have been successfully synthesized at different hydrothermal temperatures. The as-prepared NiCu alloys display a core–shell structure, which is attributed to the different reduction potentials of Ni and Cu. The unique leaflike core–shell structure of NiCu-140 exhibits outstanding microwave absorption properties compared with NiCu-120 and rodlike NiCu-160, the minimal RL is −31.13 dB at 14.3 GHz, and the absorption bandwidth (RL less than −10 dB) can reach 3.4 GHz in the frequency scope of 12.7–16.1 GHz with an absorber thickness of only 1.5 mm. This work provides an easy method to design potential and excellent electromagnetic-wave absorption materials with high-efficiency absorption, small thickness, and wide absorption bandwidths.

■ ASSOCIATED CONTENT

Ⓢ Supporting Information

TEM, HRTEM, and FESEM images. The Supporting Information is available free of charge on the ACS Publications website at DOI: 10.1021/acsami.5b02716.

■ AUTHOR INFORMATION

Corresponding Authors

*E-mail: gang_shao@zzu.edu.cn.
*E-mail: zhangray@zzia.edu.cn. Tel: +86-371-60632007. Fax: +86-371-60632600.

Notes

The authors declare no competing financial interest.

■ ACKNOWLEDGMENTS

■ REFERENCES

(1) Wang, H.; Wu, L.; Jiao, J.; Zhou, J.; Xu, Y.; Zhang, H.; Jiang, Z.; Shen, B.; Wang, Z. Covalent interaction enhanced electromagnetic wave absorption in SiC/Co hybrid nanowires. *J. Mater. Chem. A* **2015**, *3*, 6517–6525.

(2) Li, X.; Feng, J.; Du, Y.; Bai, J.; Fan, H.; Zhang, H.; Peng, Y.; Li, F. One-pot synthesis of CoFe₂O₄/graphene oxide hybrids and their conversion into FeCo/graphene hybrids for lightweight and highly efficient microwave absorber. *J. Mater. Chem. A* **2015**, *3*, 5535–5546.

(3) Singh, K.; Ohlan, A.; Pham, V. H.; R, B.; Varshney, S.; Jang, J.; Hur, S. H.; Choi, W. M.; Kumar, M.; Dhawan, S. K.; Kong, B.-S.; Chung, J. S. Nanostructured graphene/Fe₃O₄ incorporated polyaniline as a high performance shield against electromagnetic pollution. *Nanoscale* **2013**, *5*, 2411–2420.

(4) Zhao, B.; Shao, G.; Fan, B.; Zhao, W.; Chen, Y.; Zhang, R. Facile synthesis of crumpled ZnS net-wrapped Ni walnut spheres with enhanced microwave absorption properties. *RSC Adv.* **2015**, *5*, 9806–9814.

(5) Sun, D.; Zou, Q.; Wang, Y.; Wang, Y.; Jiang, W.; Li, F. Controllable synthesis of porous Fe₃O₄@ZnO sphere decorated graphene for extraordinary electromagnetic wave absorption. *Nanoscale* **2014**, *6*, 6557–6562.

(6) Tantawy, H. R.; Aston, D. E.; Smith, J. R.; Young, J. L. Comparison of Electromagnetic Shielding with Polyaniline Nanopowders Produced in Solvent-Limited Conditions. *ACS Appl. Mater. Interfaces* **2013**, *5*, 4648–4658.

(7) Lu, M.-M.; Cao, W.-Q.; Shi, H.-L.; Fang, X.-Y.; Yang, J.; Hou, Z.-L.; Jin, H.-B.; Wang, W.-Z.; Yuan, J.; Cao, M.-S. Multi-wall carbon nanotubes decorated with ZnO nanocrystals: mild solution-process synthesis and highly efficient microwave absorption properties at elevated temperature. *J. Mater. Chem. A* **2014**, *2*, 10540–10547.

(8) Gupta, T. K.; Singh, B. P.; Mathur, R. B.; Dhakate, S. R. Multi-walled carbon nanotube–graphene–polyaniline multiphase nanocomposite with superior electromagnetic shielding effectiveness. *Nanoscale* **2014**, *6*, 842–851.

(9) Yu, Z.; Yao, Z.; Zhang, N.; Wang, Z.; Li, C.; Han, X.; Wu, X.; Jiang, Z. Electric field-induced synthesis of dendritic nanostructured α-Fe for electromagnetic absorption application. *J. Mater. Chem. A* **2013**, *1*, 4571–4576.

(10) Tong, G.; Hu, Q.; Wu, W.; Li, W.; Qian, H.; Liang, Y. Submicrometer-sized NiO octahedra: facile one-pot solid synthesis, formation mechanism, and chemical conversion into Ni octahedra with excellent microwave-absorbing properties. *J. Mater. Chem.* **2012**, *22*, 17494–17504.

(11) Saini, P.; Arora, M.; Gupta, G.; Gupta, B. K.; Singh, V. N.; Choudhary, V. High permittivity polyaniline–barium titanate nanocomposites with excellent electromagnetic interference shielding response. *Nanoscale* **2013**, *5*, 4330–4336.

(12) Zhou, M.; Zhang, X.; Wei, J.; Zhao, S.; Wang, L.; Feng, B. Morphology-Controlled Synthesis and Novel Microwave Absorption Properties of Hollow Urchinlike α-MnO₂ Nanostructures. *J. Phys. Chem.C* **2011**, *115*, 1398–1402.

(13) Li, H.; Huang, Y.; Sun, G.; Yan, X.; Yang, Y.; Wang, J.; Zhang, Y. Directed Growth and Microwave Absorption Property of Crossed ZnO Netlike Micro-/Nanostructures. *J. Phys. Chem.C* **2010**, *114*, 10088–10091.

(14) Yu, Z.; Zhang, N.; Yao, Z.; Han, X.; Jiang, Z. Synthesis of hierarchical dendritic micro–nano structure CoₓFe₁₋ₓ alloy with tunable electromagnetic absorption performance. *J. Mater. Chem. A* **2013**, *1*, 12462–12470.

(15) Liu, X. G.; Geng, D. Y.; Zhang, Z. D. Microwave-absorption properties of FeCo microspheres self-assembled by Al₂O₃-coated FeCo nanocapsules. *Appl. Phys. Lett.* **2008**, *92*, 243110.

(16) Han, Z.; Li, D.; Wang, H.; Liu, X. G.; Li, J.; Geng, D. Y.; Zhang, Z. D. Broadband electromagnetic-wave absorption by FeCo/C nanocapsules. *Appl. Phys. Lett.* **2009**, *95*, 023114.

(17) Meshcheryakov, V. F.; Fetisov, Y. K.; Stashkevich, A. A.; Viau, G. Magnetic and microwave properties of nanocomposite films on the basis of Fe–Co–Ni particles of various shapes. *J. Appl. Phys.* **2008**, *104*, 063910.

(18) Yang, Y.; Xu, C.; Xia, Y.; Wang, T.; Li, F. Synthesis and microwave absorption properties of FeCo nanoplates. *J. Alloys Compd.* **2010**, *493*, 549–552.

(19) Wang, L.; He, F.; Wan, Y. Facile synthesis and electromagnetic wave absorption properties of magnetic carbon fiber coated with Fe–Co alloy by electroplating. *J. Alloys Compd.* **2011**, *509*, 4726–4730.

(20) Zhao, B.; Shao, G.; Fan, B.; Xie, Y.; Zhang, R. Preparation and electromagnetic wave absorption of chain-like CoNi by a hydrothermal route. *J. Magn. Magn. Mater.* **2014**, *372*, 195−200.

(21) Chen, X.-G.; Cheng, J.-P.; Lv, S.-S.; Zhang, P.-P.; Liu, S.-T.; Ye, Y. Preparation of porous magnetic nanocomposites using corncob powders as template and their applications for electromagnetic wave absorption. *Compos. Sci. Technol.* **2012**, *72*, 908−914.

(22) Zhang, S.; Zeng, H. C. Solution-Based Epitaxial Growth of Magnetically Responsive Cu@Ni Nanowires. *Chem. Mater.* **2010**, *22*, 1282−1284.

(23) Kumari, S.; Kumar, A.; Singh, A. P.; Garg, M.; Dutta, P. K.; Dhawan, S. K.; Mathur, R. B. Cu−Ni alloy decorated graphite layers for EMI suppression. *RSC Adv.* **2014**, *4*, 23202−23209.

(24) Nicolson, A. M.; R, G. F. Measurement of the Intrinsic Properties of Materials by Time-Domain Techniques. *IEEE Trans. Instrum. Meas.* **1970**, *19*, 377−382.

(25) Biswas, M.; Saha, A.; Dule, M.; Mandal, T. K. Polymer-Assisted Chain-like Organization of CuNi Alloy Nanoparticles: Solvent-Adoptable Pseudohomogeneous Catalysts for Alkyne−Azide Click Reactions with Magnetic Recyclability. *J. Phys. Chem.C* **2014**, *118*, 22156−22165.

(26) Rathmell, A. R.; Nguyen, M.; Chi, M.; Wiley, B. J. Synthesis of oxidation-resistant cupronickel nanowires for transparent conducting nanowire networks. *Nano Lett.* **2012**, *12*, 3193−9.

(27) Ye, J.; Chen, Q.-W.; Qi, H.-P.; Tao, N. Formation of nickel dendritic crystals with peculiar orientations by magnetic-induced aggregation and limited diffusion. *Cryst. Growth Des.* **2008**, *8*, 2464−2468.

(28) Qiu, R.; Zhang, X. L.; Qiao, R.; Li, Y.; Kim, Y. I.; Kang, Y. S. CuNi Dendritic Material: Synthesis, Mechanism Discussion, and Application as Glucose Sensor. *Chem. Mater.* **2007**, *19*, 4174−4180.

(29) Han, Y.; Fuji, M.; Shchukin, D.; Möhwald, H.; Takahashi, M. A New Model for the Synthesis of Hollow Particles via the Bubble Templating Method. *Cryst. Growth Des.* **2009**, *9*, 3771−3775.

(30) Yamauchi, T.; Tsukahara, Y.; Yamada, K.; Sakata, T.; Wada, Y. Nucleation and Growth of Magnetic Ni−Co (Core−Shell) Nanoparticles in a One-Pot Reaction under Microwave Irradiation. *Chem. Mater.* **2011**, *23*, 75−84.

(31) Zhang, S.; Zeng, H. C. Self-Assembled Hollow Spheres of β-Ni(OH)$_2$ and Their Derived Nanomaterials. *Chem. Mater.* **2009**, *21*, 871−883.

(32) Chang, Y.; Lye, M. L.; Zeng, H. C. Large-Scale Synthesis of High-Quality Ultralong Copper Nanowires. *Langmuir* **2005**, *21*, 3746−3748.

(33) Yamauchi, T.; Tsukahara, Y.; Sakata, T.; Mori, H.; Yanagida, T.; Kawai, T.; Wada, Y. Magnetic Cu−Ni (core−shell) nanoparticles in a one-pot reaction under microwave irradiation. *Nanoscale* **2010**, *2*, 515−523.

(34) Zhao, B.; Shao, G.; Fan, B.; Zhao, W.; Zhang, R. Investigation of the electromagnetic absorption properties of Ni@TiO$_2$ and Ni@SiO$_2$ composite microspheres with core−shell structure. *Phys. Chem. Chem. Phys.* **2015**, *17*, 2531−2539.

(35) Wang, L.; Huang, Y.; Li, C.; Chen, J.; Sun, X. Hierarchical graphene@Fe$_3$O$_4$ nanocluster@carbon@MnO$_2$ nanosheet array composites: synthesis and microwave absorption performance. *Phys. Chem. Chem. Phys.* **2015**, *17*, 5878−5886.

(36) Wang, L.; Huang, Y.; Sun, X.; Huang, H.; Liu, P.; Zong, M.; Wang, Y. Synthesis and microwave absorption enhancement of graphene@Fe$_3$O$_4$@SiO$_2$@NiO nanosheet hierarchical structures. *Nanoscale* **2014**, *6*, 3157−3164.

(37) Ma, F.; Qin, Y.; Li, Y.-Z. Enhanced microwave performance of cobalt nanoflakes with strong shape anisotropy. *Appl. Phys. Lett.* **2010**, *96*, 202507.

(38) Yuan, L.; Xiang Xuan, L.; Rong, L.; Ying, L. Fabrication and electromagnetic wave absorption of novel Ni$_{0.4}$Zn$_{0.2}$Mn$_{0.4}$Ce$_{0.06}$Fe$_{1.94}$O$_4$-carbonyl iron composites. *RSC Adv.* **2015**, *5*, 18660−18665.

(39) Liu, X. G.; Jiang, J. J.; Geng, D. Y.; Li, B. Q.; Han, Z.; Liu, W.; Zhang, Z. D. Dual nonlinear dielectric resonance and strong natural

resonance in Ni/ZnO nanocapsules. *Appl. Phys. Lett.* **2009**, *94*, 053119.

(40) Tong, G.; Yuan, J.; Wu, W.; Hu, Q.; Qian, H.; Li, L.; Shen, J. Flower-like Co superstructures: Morphology and phase evolution mechanism and novel microwave electromagnetic characteristics. *CrystEngComm* **2012**, *14*, 2071−2079.

(41) Wang, G.-S.; Wu, Y.; Wei, Y.-Z.; Zhang, X.-J.; Li, Y.; Li, L.-D.; Wen, B.; Yin, P.-G.; Guo, L.; Cao, M.-S. Fabrication of Reduced Graphene Oxide (RGO)/Co$_3$O$_4$ Nanohybrid Particles and a RGO/Co$_3$O$_4$/Poly(vinylidene fluoride) Composite with Enhanced Wave-Absorption Properties. *ChemPlusChem* **2014**, *79*, 375−381.

(42) Wang, H.; Guo, H.; Dai, Y.; Geng, D.; Han, Z.; Li, D.; Yang, T.; Ma, S.; Liu, W.; Zhang, Z. Optimal electromagnetic-wave absorption by enhanced dipole polarization in Ni/C nanocapsules. *Appl. Phys. Lett.* **2012**, *101*, 083116.

(43) Yang, H.-J.; Cao, W.-Q.; Zhang, D.-Q.; Su, T.-J.; Shi, H.-L.; Wang, W.-Z.; Yuan, J.; Cao, M.-S. NiO Hierarchical Nanorings on SiC: Enhancing Relaxation to Tune Microwave Absorption at Elevated Temperature. *ACS Appl. Mater. Interfaces* **2015**, *7*, 7073−7077.

(44) Cao, M.-S.; Yang, J.; Song, W.-L.; Zhang, D.-Q.; Wen, B.; Jin, H.-B.; Hou, Z.-L.; Yuan, J. Ferroferric Oxide/Multiwalled Carbon Nanotube vs Polyaniline/Ferroferric Oxide/Multiwalled Carbon Nanotube Multiheterostructures for Highly Effective Microwave Absorption. *ACS Appl. Mater. Interfaces* **2012**, *4*, 6949−6956.

(45) Shi, Z.-c.; Fan, R.-h.; Zhang, Z.-d.; Qian, L.; Gao, M.; Zhang, M.; Zheng, L.-t.; Zhang, X.-h.; Yin, L.-w. Random Composites of Nickel Networks Supported by Porous Alumina Toward Double Negative Materials. *Adv. Mater.* **2012**, *24*, 2349−2352.

(46) Shi, X.-L.; Cao, M.-S.; Yuan, J.; Fang, X.-Y. Dual nonlinear dielectric resonance and nesting microwave absorption peaks of hollow cobalt nanochains composites with negative permeability. *Appl. Phys. Lett.* **2009**, *95*, 163108.

(47) Guan, P. F.; Zhang, X. F.; Guo, J. J. Assembled Fe$_3$O$_4$ nanoparticles on graphene for enhanced electromagnetic wave losses. *Appl. Phys. Lett.* **2012**, *101*, 153108.

(48) He, S.; Lu, C.; Wang, G.-S.; Wang, J.-W.; Guo, H.-Y.; Guo, L. Synthesis and Growth Mechanism of White-Fungus-Like Nickel Sulfide Microspheres, and Their Application in Polymer Composites with Enhanced Microwave-Absorption Properties. *ChemPlusChem* **2014**, *79*, 569−576.

(49) Zhao, B.; Shao, G.; Fan, B.; Zhao, W.; Xie, Y.; Zhang, R. ZnS nanowall coated Ni composites: facile preparation and enhanced electromagnetic wave absorption. *RSC Adv.* **2014**, *4*, 61219−61225.

(50) Wang, G.; Gao, Z.; Wan, G.; Lin, S.; Yang, P.; Qin, Y. High densities of magnetic nanoparticles supported on graphene fabricated by atomic layer deposition and their use as efficient synergistic microwave absorbers. *Nano Res.* **2014**, *7*, 704−716.

(51) Yu, H.; Wang, T.; Wen, B.; Lu, M.; Xu, Z.; Zhu, C.; Chen, Y.; Xue, X.; Sun, C.; Cao, M. Graphene/polyaniline nanorod arrays: synthesis and excellent electromagnetic absorption properties. *J. Mater. Chem.* **2012**, *22*, 21679−21685.

(52) Han, M.; Yin, X.; Kong, L.; Li, M.; Duan, W.; Zhang, L.; Cheng, L. Graphene-wrapped ZnO hollow spheres with enhanced electromagnetic wave absorption properties. *J. Mater. Chem. A* **2014**, *2*, 16403−16409.

(53) Fang, P. H. Cole—Cole Diagram and the Distribution of Relaxation Times. *J. Chem. Phys.* **1965**, *42*, 3411−3413.

(54) Cao, M.-S.; Song, W.-L.; Hou, Z.-L.; Wen, B.; Yuan, J. The effects of temperature and frequency on the dielectric properties, electromagnetic interference shielding and microwave-absorption of short carbon fiber/silica composites. *Carbon* **2010**, *48*, 788−796.

(55) Liu, J.; Cao, W.-Q.; Jin, H.-B.; Yuan, J.; Zhang, D.-Q.; Cao, M.-S. Enhanced permittivity and multi-region microwave absorption of nanoneedle-like ZnO in the X-band at elevated temperature. *J. Mater. Chem. C* **2015**, *3*, 4670−4677.

(56) Wen, B.; Cao, M.-S.; Hou, Z.-L.; Song, W.-L.; Zhang, L.; Lu, M.-M.; Jin, H.-B.; Fang, X.-Y.; Wang, W.-Z.; Yuan, J. Temperature dependent microwave attenuation behavior for carbon-nanotube/silica composites. *Carbon* **2013**, *65*, 124−139.

(57) Liu, Y.; Liu, X.; Li, R.; Wen, W.; Wang, X. Design and fabrication of carbon fiber/carbonyl iron core−shell structure composites as high-performance microwave absorbers. *RSC Adv.* **2015**, *5*, 8713−8720.

(58) Wu, M.; Zhang, Y. D.; Hui, S.; Xiao, T. D.; Ge, S.; Hines, W. A.; Budnick, J. I.; Taylor, G. W. Microwave magnetic properties of Co_{50}/$(SiO_2)_{50}$ nanoparticles. *Appl. Phys. Lett.* **2002**, *80*, 4404−4406.

(59) Zhang, X. F.; Dong, X. L.; Huang, H.; Liu, Y. Y.; Wang, W. N.; Zhu, X. G.; Lv, B.; Lei, J. P.; Lee, C. G. Microwave absorption properties of the carbon-coated nickel nanocapsules. *Appl. Phys. Lett.* **2006**, *89*, 053115.

(60) Guo, J.; Wang, X.; Miao, P.; Liao, X.; Zhang, W.; Shi, B. One-step seeding growth of controllable Ag@Ni core−shell nanoparticles on skin collagen fiber with introduction of plant tannin and their application in high-performance microwave absorption. *J. Mater. Chem.* **2012**, *22*, 11933−11942.

(61) Zhao, B.; Shao, G.; Fan, B.; Zhao, W.; Zhang, R. Fabrication and enhanced microwave absorption properties of Al_2O_3 nanoflake-coated Ni core−shell composite microspheres. *RSC Adv.* **2014**, *4*, 57424−57429.

(62) Wang, G.; Peng, X.; Yu, L.; Wan, G.; Lin, S.; Qin, Y. Enhanced microwave absorption of ZnO coated with Ni nanoparticles produced by atomic layer deposition. *J. Mater. Chem. A* **2015**, *3*, 2734−2740.

(63) Zhou, W.; Hu, X.; Bai, X.; Zhou, S.; Sun, C.; Yan, J.; Chen, P. Synthesis and Electromagnetic, Microwave Absorbing Properties of Core−Shell Fe_3O_4−Poly(3,4-ethylenedioxythiophene) Microspheres. *ACS Appl. Mater. Interfaces* **2011**, *3*, 3839−3845.

(64) Zhao, B.; Shao, G.; Fan, B.; Zhao, W.; Zhang, R. Facile synthesis and enhanced microwave absorption properties of novel hierarchical heterostructures based on a Ni microsphere−CuO nano-rice core−shell composite. *Phys. Chem. Chem. Phys.* **2015**, *17*, 6044−6052.

(65) Wang, C.; Han, X.; Zhang, X.; Hu, S.; Zhang, T.; Wang, J.; Du, Y.; Wang, X.; Xu, P. Controlled Synthesis and Morphology-Dependent Electromagnetic Properties of Hierarchical Cobalt Assemblies. *J. Phys. Chem. C* **2010**, *114*, 14826−14830.